EES Batteries

PAPER

View Article Online
View Journal

Cite this: DOI: 10.1039/d5eb00208g

Breaking solvation compactness: methyl acetate cosolvent engineering enables high-voltage lithium metal batteries at low temperatures

Hui Tian,[a] Yufeng Luo,*[b] Zixin Hong,[a] Zhenhan Fang,[a] Hengcai Wu,[a] Fei Zhao,[a] Guoqiang Tan,[b] Qunqing Li,[a,c] Shoushan Fan[a] and Jiaping Wang *[a,c]

Received 26th October 2025,
Accepted 16th March 2026

DOI: 10.1039/d5eb00208g

rsc.li/EESBatteries

State-of-the-art lithium metal batteries (LMBs) offer exceptional energy density for next-generation energy storage. Yet, their practical application is hindered by unstable cathode–electrolyte interphases (CEIs) under high-voltage conditions and sluggish ionic transport kinetics at low temperatures. Here, we develop a small linear molecule, methyl acetate (MA), as a cosolvent in a fluorinated-based electrolyte (FBE) to address these challenges. MA presents a high binding energy with Li ions and weak repulsive interactions with fluorinated solvent molecules and PF_6^- anions. Consequently, small MA molecules can participate in the inner solvation sheath and disrupt the compact solvation structure constructed by fluorinated solvent molecules, thereby contributing to the generation of robust and stable CEIs and bulk electrolytes with superior Li^+ transport kinetics. Based on the well-formulated MA-FBEs, the assembled $LiNi_{0.8}Co_{0.1}Mn_{0.1}O_2$||Li full cells with a low N/P ratio of 2 can stably operate under high voltage (181.2 mAh g^{-1} at 4.8 V), deliver high rate capability (142.8 mAh g^{-1} at 10C), and maintain excellent low-temperature performance (159.1 mAh g^{-1} at 0.05C and 99.1 mAh g^{-1} at 0.1C at −70 °C), demonstrating the industrial viability of this developed electrolyte.

Broader context

Lithium metal batteries (LMBs) lead in high-energy-density storage technologies, but their practical application under high-voltage and low-temperature conditions remains hindered. Strategies like high-concentration electrolytes (HCEs) and localized high-concentration electrolytes (LHCEs) have been tested to address LMB challenges. They suffer from trade-offs such as high viscosity and insufficient Li^+ dissociation, however, and fail to provide a comprehensive solution. Fluorinated-based electrolytes (FBEs) have thus been adopted as an alternative, yet they still have critical limitations. These include brittle, inorganic-rich cathode–electrolyte interphases (CEIs) and compact solvation structures that impede ionic transport. A cost-effective optimization targets these FBE-specific flaws using methyl acetate (MA) as a cosolvent. This improvement enables LMBs with a low N/P ratio of 2 to achieve exceptional cycling stability under 4.8 V high voltage, 10C high rate, and −70 °C ultralow temperature. It provides an innovative and commercially viable solution for the development of next-generation high-performance LMBs in extreme environments.

1. Introduction

State-of-the-art lithium metal batteries (LMBs) fail to meet most of the extreme working conditions required for future high-energy-density energy storage systems. This is mainly due to the limited electrochemical window (≤4.3 V) of conventional ester-based electrolytes and their narrow operating temperature range (−20 to 40 °C).[1–4] Specifically, the electrochemical degradation of conventional ester-based electrolytes under high-voltage operation leads to the formation of an undesired cathode–electrolyte interphase (CEI) with poor mechanical properties and impaired ionic transport.[5–8] As a result, the energy density and capacity retention of the LMBs both deteriorate.[9,10] Additionally, extreme operating temperatures in practical applications negatively impact the electrochemical performance of LMBs, especially at low temperatures (below −20 °C). The inherently strong coordination in solvation shells significantly reduces Li^+ conductivity in the bulk electrolyte, resulting in sluggish transport kinetics.[8,11,12] Recent progress in advanced solvation chemistry has established that precise regulation of the electrolyte solvation structure provides a critical guideline to simultaneously tackle high-voltage interfacial degradation and sluggish ionic transport kinetics in high-performance rechargeable batteries.[13]

[a]Department of Physics and Tsinghua-Foxconn Nanotechnology Research Center, Tsinghua University, Beijing, 100084, China. E-mail: jpwang@tsinghua.edu.cn
[b]School of Materials Science and Engineering, Beijing Institute of Technology, Beijing, 100081, PR China. E-mail: luoyf@bit.edu.cn
[c]Frontier Science Center for Quantum Information, Beijing, 100084, China

Therefore, it is essential to develop effective strategies to create an electrolyte that can form stable and robust CEIs while ensuring excellent Li^+ transport kinetics at low temperatures.

Electrolyte engineering has proven effective in addressing the issues discussed above, mainly through the use of high-concentration electrolytes (HCEs) and localized high-concentration electrolytes (LHCEs).[14–17] HCEs and LHCEs can reduce the number of free solvent molecules and encourage more anions to participate in CEI formation by increasing the salt/solvent ratios. Specifically, the contact ion pairs (CIP) and aggregates (AGG) of the ionic species increase, while solvent-separated ion pairs (SSIP) decrease significantly.[18,19] The CEIs formed from such regulated-solvated electrolytes are typically rich in inorganic components with high ionic conductivity and Young's modulus, providing a robust kinetic barrier to suppress parasitic reactions at the cathode-electrolyte interface.[20,21] However, HCEs are often hampered by high viscosity and poor wettability, whereas LHCEs tend to exhibit lower ionic conductivity due to diluent-encapsulated Li^+ solvation sheaths.[18,22,23] Moreover, the reliance on organic Li salts hinders efforts to reduce costs.

Weakly solvating electrolytes (WSEs) offer a promising solution to the limitations of HCEs and LHCEs by enabling anion-rich solvation structures through solvents with diminished electron-donating capacity, thereby achieving both low viscosity and enhanced ionic conductivity.[24–26] However, most of the WSEs are ether-based, and their instability at voltages above 4.5 V restricts their ability to improve the energy density of LMBs. Among the various WSEs, fluorinated-based electrolytes (FBEs), which are ester-based, have emerged as a promising alternative. The presence of carbon–fluorine (C–F) bonds in FBEs imparts high chemical and oxidation stability, effectively suppressing their degradation and extending the operational voltage window of LMBs.[27,28] Additionally, the incorporation of fluorine (F) facilitates the formation of rigid and stable lithium fluoride (LiF)-rich CEIs with high Li^+ transport capability.[29,30] However, LiF-rich CEIs exhibit insufficient resilience to volumetric changes under extreme conditions, such as deep (de) lithiation, due to the intrinsic brittleness of LiF. This can induce interfacial structure and bulk phase transitions.[31,32] For another, the strong electronegativity of F atoms in the fluorinated solvents (3.98, compared to 2.20 for hydrogen (H)) promotes strong intermolecular electrostatic interactions and hydrogen bonding, while strengthening ion–dipole interactions between anions and solvent molecules, leading to the formation of a compact solvation structure with large ionic clusters in bulk FBEs.[33] As a result, the ionic conductivity of the FBEs is severely restricted, facing significant challenges in applications at low temperatures (below −30 °C).[34–36] Although the use of organic salts (*e.g.*, lithium bis(fluorosulfonyl)imide, LiFSI), coupled with additives (*e.g.*, lithium difluoro(oxalato)borate, LiDFOB), can address the problems discussed above, the high cost of these salts and the fluorinated solvents still makes FBEs difficult to commercialize.[37–39]

To address issues with FBEs, it is essential to improve the elasticity of the generated CEIs while disrupting the compact solvation structures of FBEs. In this proof-of-concept study, we introduce methyl acetate (MA) as a cosolvent (40 vol%) into an FBE composed of fluoroethylene carbonate (FEC) and methyl (2,2,2-trifluoroethyl)carbonate (FEMC) with inorganic salt lithium hexafluorophosphate ($LiPF_6$). In the developed MA-FBE electrolyte, the MA molecules participate in the inner solvation sheath of Li^+ due to their minimal steric hindrance and higher binding energy. Coupled with the higher highest occupied molecular orbital (HOMO) energy level of the MA molecules, more organic components are formed in the CEI layer, enhancing its elasticity. More importantly, the MA molecules exhibit slight repulsive forces toward fluorinated solvent molecules and PF_6^- anions, along with their high mobility, which effectively loosens the compact solvation structure of FBEs and promotes the dynamic transport of large ion clusters. This leads to a significant improvement in Li^+ conductivity in the bulk electrolyte. As a result, LMBs using MA-FBEs demonstrate overall enhancements in high-voltage, high-rate, and wide-temperature performance when paired with $LiNi_{0.8}Co_{0.1}Mn_{0.1}O_2$ (NCM811) cathodes. Specifically, the assembled NCM811‖Li full cell with a low N/P ratio of 2 maintains a capacity of 134.8 mAh g^{-1} after 200 cycles under ultra-high voltage (4.8 V) and high-rate (5C) conditions at room temperature. Additionally, the full cell performs well at −70 °C, with specific capacities of 159.1 and 99.1 mAh g^{-1} at 0.05C and 0.1C, respectively. It also maintains stable cycling over 200 cycles with capacity retentions of 84.6% (0.1C) and 84.1% (0.2C) at −40 °C. The MA-FBE also enables NCM811 (3.0 mAh cm^{-2})‖Li (50 μm) pouch cells to achieve a high energy density of 275.9 Wh kg^{-1}, with around 90% capacity retention after 100 cycles under practical conditions, further confirming the industrial viability of the developed electrolyte.

2. Results and discussion

2.1. Solvation structure engineering and spatial dimension analysis

Fluorine atoms, with their high electronegativity on the Pauling scale, cause significant intramolecular charge redistribution in solvent molecules due to their strong electron-withdrawing nature.[33] Density functional theory (DFT) calculations of electrostatic potential (ESP) distributions for representative carbonates, carboxylates, and their fluorinated derivatives (Fig. S1 and Table S1) show that fluorine substitution decreases electron density around the carbonyl oxygen, raising ESP_{min} and thereby weakening Li^+ solvation. This aids in developing weakly solvating electrolytes. However, fluorination also raises ESP_{max} at molecular surfaces, strengthening ion–dipole interactions between anions and solvent molecules. Along with considerable steric hindrance caused by the larger van der Waals radius of fluorine atoms, these factors collectively lead to the formation of rigid, large ionic clusters in fluorinated electrolytes. Such structures greatly hinder Li^+ transport, especially at low temperatures, resulting in poor ionic conductivity.

To address these limitations, we incorporate MA into the FBE baseline electrolyte. MA exhibits a wide liquid range (−98 to 57 °C), an ultralow viscosity (0.37 mPa s), and a relatively low ESP_{max} (<20 kcal mol^{-1}), enabling dynamic solvation structure optimization across a broad temperature range (Table S1). Molecular dynamics (MD) simulations of the FBE and MA-FBE electrolytes were conducted to elucidate the role of MA in regulating solvation. Radial distribution functions (RDFs) and coordination numbers (CNs) of Li^+, calculated using a 3 Å cutoff radius for the primary solvation shell, showed that the F CN of PF_6^- with Li^+ in FBE was 2.16 at 25 °C, slightly decreasing to 2.12 in MA-FBE (Fig. 1a and b). For the oxygen (O) CN of fluorinated solvents with Li^+, the values for FEC and FEMC in FBE were 2.15 and 1.44, respectively, which dropped to 1.52 (FEC) and 0.78 (FEMC) in MA-FBE. These quantitative reductions directly reflect the diminished occupation of fluorinated solvents in the Li^+ primary solvation sheath. Significantly, MA partially displaces FEC/FEMC molecules, contributing an O CN of 1.38 with Li^+. Collectively, these distinct CN variations provide quantitative evidence for the effective disruption of the compact solvation structure constructed by fluorinated solvents.

Temperature-dependent studies (−70 °C and 60 °C) further confirmed its solvation structural consistency, with similar coordination patterns maintained (Fig. S2). Binding energy (ΔE) calculations showed that FEC and FEMC exhibited weak attraction to PF_6^- (−32.533 and −4.658 kJ mol^{-1}), indicating a preference for forming compact ionic clusters (Fig. 1c).

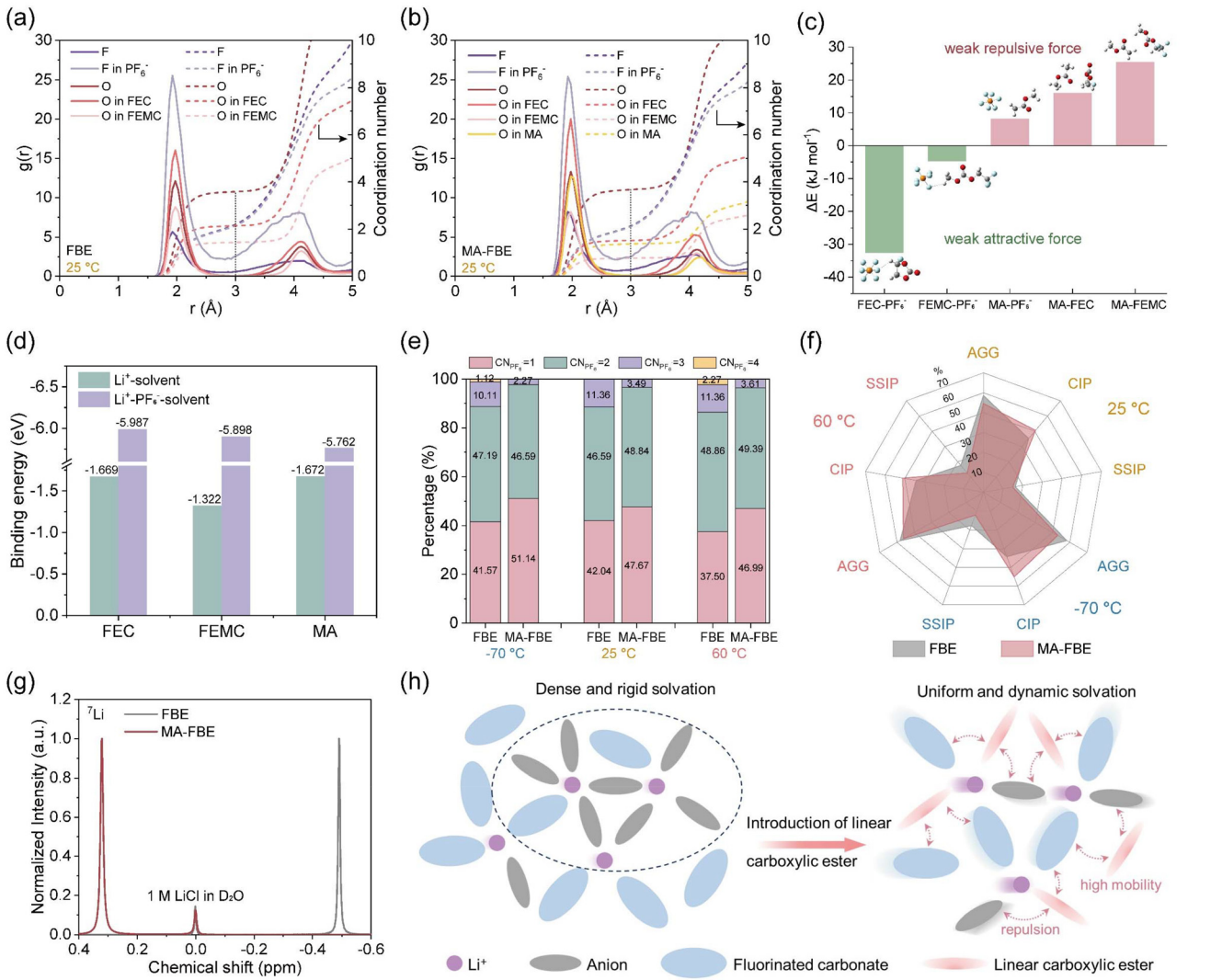

Fig. 1 Electrolyte design strategies. RDFs and CNs for the (a) FBE and (b) MA-FBE electrolytes at 25 °C (Fig. S2 for RDFs and CNs at −70 °C and 60 °C); (c) binding energies between FEC/FEMC and PF_6^-, as well as between MA and PF_6^-/FEC/FEMC; (d) binding energies between Li^+ and solvent molecules, as well as among Li^+, PF_6^- and solvent molecules; (e) $CN_{PF_6^-}$ distribution of the FBE and MA-FBE electrolytes at −70 °C, 25 °C, and 60 °C; (f) radar charts of the SSIP, CIP, and AGG proportions in the two electrolytes at −70 °C, 25 °C, and 60 °C; (g) ^7Li NMR spectra of the FBE and MA-FBE electrolytes; (h) schematic diagram illustrating the solvation structures in fluorinated electrolytes before and after the introduction of linear carboxylic esters.

Interestingly, MA demonstrated weak repulsion with PF_6^- (+8.155 kJ mol^{-1}), FEC (+16.073 kJ mol^{-1}), and FEMC (+25.470 kJ mol^{-1}). Further analysis of binding energies between Li^+ and solvent molecules revealed that MA (−1.672 eV) has a slightly stronger interaction than FEC (−1.669 eV) and FEMC (−1.322 eV). Conversely, when considering ternary interactions involving Li^+, PF_6^-, and solvent molecules, MA (−5.762 eV) showed weaker binding compared to FEC (−5.987 eV) and FEMC (−5.898 eV), which is due to its weak repulsion with PF_6^- (Fig. 1d). This implies that MA can disrupt the compact solvation structures formed by fluorinated solvents, thereby promoting spatial uniformity.

We then quantified anion coordination numbers ($CN_{PF_6^-}$) in the primary solvation shell of Li^+ at −70, 25, and 60 °C (Fig. 1e). The FBE system exhibited significant $CN_{PF_6^-}$ = 3 coordination (>10%) and even detectable $CN_{PF_6^-}$ = 4 configurations. Upon introducing MA, the $CN_{PF_6^-}$ = 3 coordination decreased markedly (<4%), and $CN_{PF_6^-}$ = 4 configurations disappeared, replaced by an increase in $CN_{PF_6^-}$ = 1 coordination. Additionally, MA-FBE exhibited a higher proportion of CIP and lower fractions of SSIP and AGG compared to FBE (Fig. 1f). These computational results collectively suggest that the MA-FBE promotes a more uniform distribution of anions in Li^+ solvation structures. Experimentally, the downfield shift from −0.49 ppm (FBE) to +0.32 ppm (MA-FBE) in ^{7}Li NMR and reduced attenuated total reflectance-Fourier transform infrared spectroscopy (ATR-FTIR) signals for Li^+-coordinated PF_6^- further support the conjecture of weakened anion shielding and decreased electron cloud density around Li^+ (Fig. 1g and S4).[40,41] Furthermore, ^{19}F NMR spectra (Fig. S5) reveal that the characteristic fluorine signals of the PF_6^- anion, FEC, and FEMC in MA-FBE all exhibit downfield shifts of 0.41 ppm, 0.34 ppm, and 0.40 ppm, respectively, which demonstrates that the introduction of MA drives the conversion of the dominant compact, strongly-bound AGG state to the weakly-bound CIP state in the electrolyte. In brief, the low molecular weight and linear structure of MA molecules enable them to integrate into the inner solvation sheath of the FBE electrolytes, alleviating steric hindrance through weak repulsive interactions. This effectively loosens the compact solvation structure of the fluorinated electrolyte and enhances Li^+ transport kinetics (Fig. 1h).

2.2. CEI analysis and bulk characterization of NCM811 cathodes

To clarify the CEI components formed in the FBE and MA-FBE, an in-depth X-ray photoelectron spectroscopy (XPS) depth-profiling analysis was first carried out on cycled NCM811 cathodes (Fig. 2a–c). The FBE-derived CEI primarily consisted of inorganic components, mainly LiF, which is predominantly produced by the decomposition of $LiPF_6$. Notably, the F 1s spectrum showed a significantly higher LiF signal compared to C–F, confirming the inorganic-rich nature of the FBE-derived CEI. Moreover, XPS depth-profiles revealed M–O and C–M (M = Ni/Co/Mn) signals in the FBE-derived CEI, indicating lattice oxygen oxidation at crack sites or the coordination of dissolved transition metal ions with oxygen species.[42] In contrast, MA-FBE caused an increase in organic components within the CEI layer (Fig. 2d and e), as evidenced by the larger C atomic ratios and the strong C–C/C–H signals in C 1s and C–O signals in O 1s.[43,44] More importantly, no detectable M–O or C–M signals appeared in the MA-FBE-derived CEI, suggesting effective suppression of transition metal ions dissolution and structural damage in the NCM811 lattice. This stabilization is attributed to the participation of MA molecules in the inner Li^+ solvation sheath, enabling the formation of a balanced organic–inorganic CEI layer that establishes a stable foundation.

The time-of-flight secondary ion mass spectrometry (ToF-SIMS) depth profiles were highly consistent with the XPS results, jointly confirming the structural characteristics of the CEI formed in the MA-FBE electrolyte (Fig. 2f and S6, S7). Compared with the FBE system, the MA-FBE-derived CEI was significantly thinner, as evidenced by the faster increase of the NiO_2^- and NiO^- signals upon sputtering. Meanwhile, the significantly enhanced intensities of oxygen-containing inorganic markers (O^-, LiO_2^-, $LiO_2H_2^-$) and MA-derived organic characteristic fragments (CH^-, C_2H^-, C_2HO^- and $C_2H_3O^-$) in the MA-FBE system verified the enrichment of organic species and lithium-rich oxide components within the CEI, which accounted for the high ionic conductivity and superior mechanical elasticity of the interphase. In contrast, the lower intensities and faster attenuation of F^-, LiF_2^- and $Li_2F_3^-$ confirmed the reduced LiF content in the MA-FBE-derived CEI. These results demonstrated that the introduction of MA effectively tailored the CEI composition by suppressing excessive LiF formation and promoting the construction of a thin, balanced organic–inorganic interphase with enriched organic components and abundant lithium-rich oxides, which was favorable for reducing interfacial resistance and suppressing structural degradation of the NCM811 cathodes.

DFT calculations further supported these findings: MA exhibited a higher HOMO energy (−7.788 eV) compared to FEC (−8.972 eV), FEMC (−8.762 eV), and $LiPF_6$ (−10.723 eV), indicating its preferential oxidation at the cathode surface (Fig. 2g).[45] Collectively, these results demonstrate that MA incorporation facilitates the formation of a robust organic–inorganic hybrid CEI, which mitigates the transition metal ions dissolution and lattice distortion during the Li intercalation/deintercalation process.

Coherently, transmission electron microscopy (TEM) analysis revealed the formed nanostructural features of CEIs in the FBE and MA-FBE. FBE yielded a non-uniform CEI (varying from 8 to 20 nm) with severe cation mixing and loss of the NCM811 layered structure (Fig. 3a), which is consistent with the XPS results. In contrast, a thin and uniform CEI of ~3 nm was generated in MA-FBE, preserving the NCM811 bulk crystallinity while forming only a sub-2 nm disordered layer (Fig. 3b).[46,47] X-ray diffraction (XRD) patterns further showed a pronounced (003) peak shift for cycled NCM811 in FBE, which was absent in MA-FBE (Fig. 3c and S8). Consequently, NCM811 particles retained their structural integrity in MA-FBE, whereas extensive cracks were observed for NCM811 cycled in FBE *via*

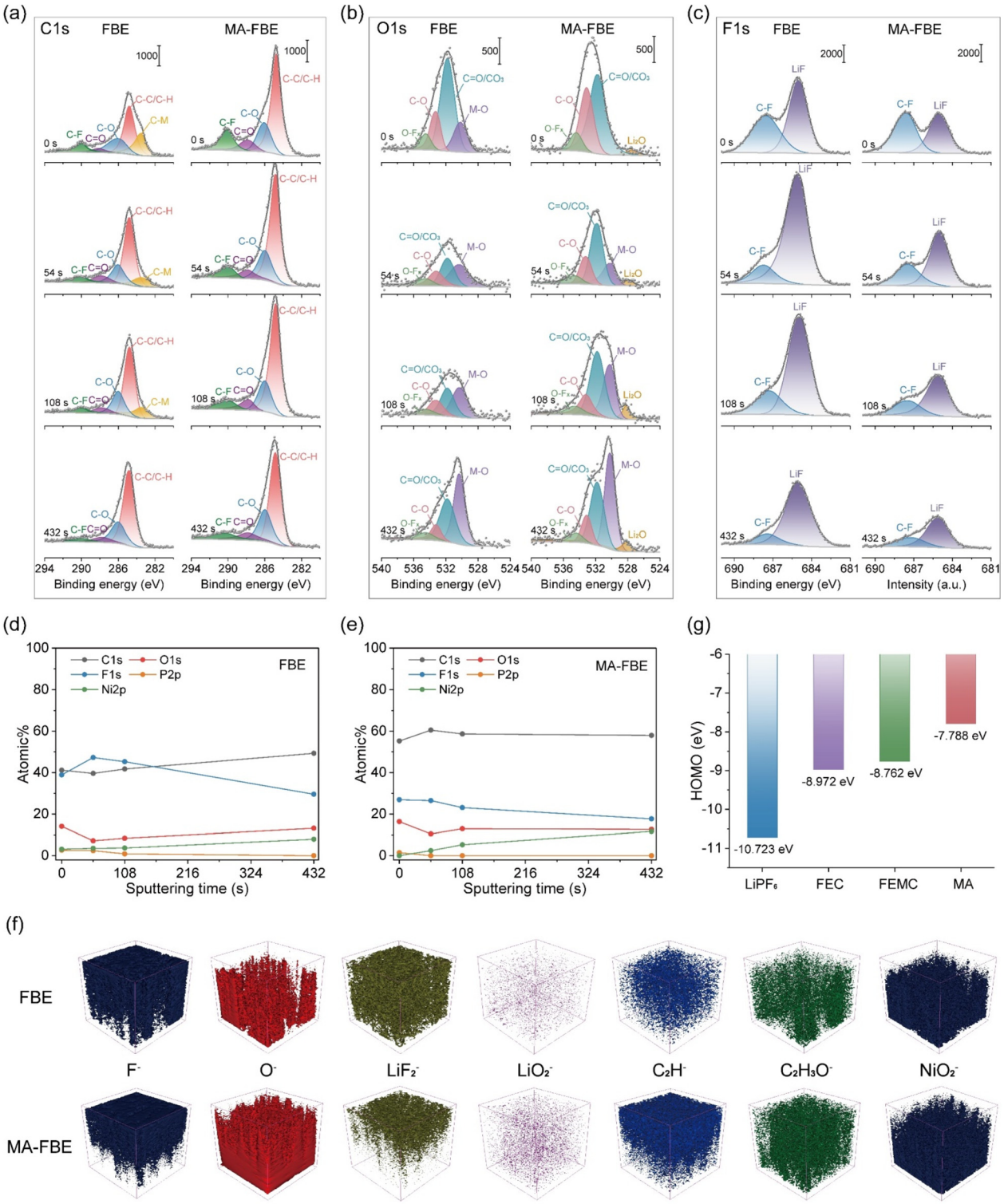

Fig. 2 CEI formation mechanisms and chemical composition. XPS (a) C 1s, (b) O 1s, and (c) F 1s spectra of the CEI on the cycled-NCM811 cathodes; XPS survey spectra of the CEI for the (d) FBE and (e) MA-FBE electrolytes; (f) 3D ToF-SIMS chemical reconstruction images of the CEI components on the cycled NCM811 cathodes; (g) computed HOMO energies of $LiPF_6$, FEC, FEMC, and MA.

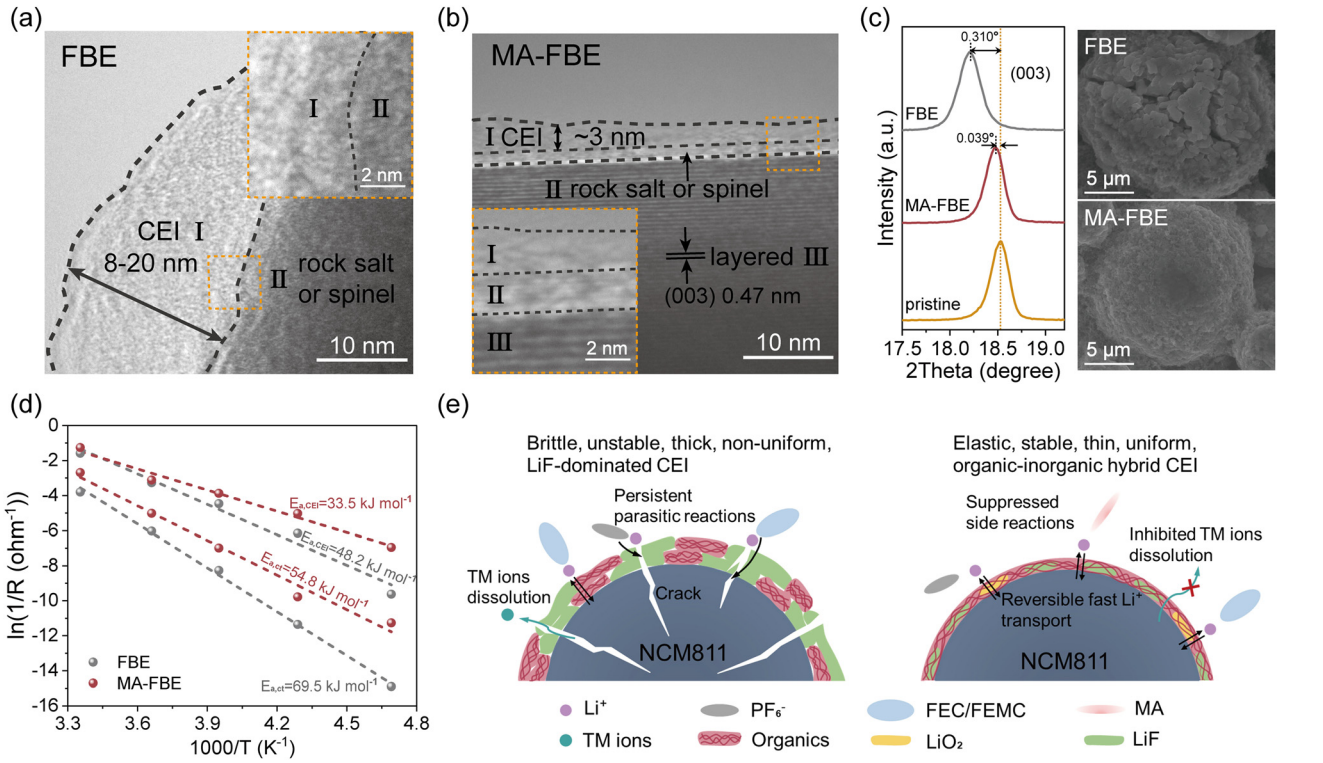

Fig. 3 Electrolyte-NCM811 interfacial properties. TEM images of cycled-NCM811 cathodes with the (a) FBE and (b) MA-FBE electrolytes; (c) XRD patterns and SEM images of cycled-NCM811 cathodes; (d) activation energy for the charge transfer process and Li^+ transport through CEI; (e) schematic illustration of the interfaces between the FBE/MA-FBE electrolytes and the NCM811 cathodes.

scanning electron microscopy (SEM). These findings directly link the CEI properties to the cycling stability.[43,48]

Moreover, electrochemical impedance spectroscopy (EIS) analysis across varying temperatures revealed lower charge transfer activation energy ($E_{a,ct}$, 54.8 *vs.* 69.5 kJ mol^{-1}) and Li^+ transport activation energy across the CEI ($E_{a,CEI}$, 33.5 *vs.* 48.2 kJ mol^{-1}) in MA-FBE, indicating reduced interfacial energy barriers and polarization during wide-temperature cycling (Fig. 3d and S9, S10).[49,50] These results demonstrate that the incorporation of MA into the electrolyte not only stabilizes the cathode and prevents cation mixing but also maintains fast Li^+ transport kinetics during cycling (Fig. 3e).

A similar stabilizing effect is anticipated at the Li anode, where MA-FBE-derived solid-electrolyte interphase (SEI) regulation is also critical to the electrochemical performance. XPS depth-profiles revealed that the inner MA-FBE-derived SEI layer was enriched with inorganic Li_2O, while the outer layer retained a LiF-dominant composition among the inorganic components (Fig. S11 and S12). Such a gradient structure significantly improves Li^+ transport kinetics and anode stability.[51–53] In contrast, the FBE-derived SEI is dominated by excessive LiF with only a weak Li_2O signal detected across the entire interphase, whose inherent brittleness directly causes SEI fracture and continuous interfacial degradation during cycling. Cu||Li half cells employing MA-FBE also demonstrated superior cycling reversibility, achieving a high and stable coulombic efficiency (CE) of 97.3% over 150 cycles. In contrast, cells with FBE exhibited lower initial CE values in the first 15 cycles and pronounced fluctuations after 105 cycles (Fig. S13). These results demonstrate the dual role of MA in stabilizing both the NCM811 cathode *via* CEI regulation and the Li anode through SEI engineering, thereby enabling long-term cycling stability in high-voltage LMBs.

2.3. Dynamic analysis of electrolyte solvation structures

Conventional spatial static analyses of solvation structures only provide equilibrium-averaged snapshots, overlooking the crucial role of dynamic solvation shell evolution in Li^+ transport mechanisms. To address this limitation, we further introduce a temporal dynamic dissection of electrolyte solvation structures, representing a methodological advance in solvation research. First, we computed the mean squared displacement (MSD) of electrolyte components to quantify the microscopic diffusion behaviors of Li^+, PF_6^-, FEC, FEMC, and MA (Fig. 4a and S14). Using the Einstein relation, the derived diffusion coefficients (D) from linear fits to MSD–time curves establish direct links between microscopic kinetics and macroscopic transport properties (Fig. 4b).[54,55] The linear small-molecule MA exhibited the highest diffusivity, with the steepest MSD slopes and largest D values across temperatures from −70 to 60 °C. Furthermore, MA-FBE showed markedly enhanced MSD slopes and D values for Li^+, PF_6^-, FEC, and FEMC components

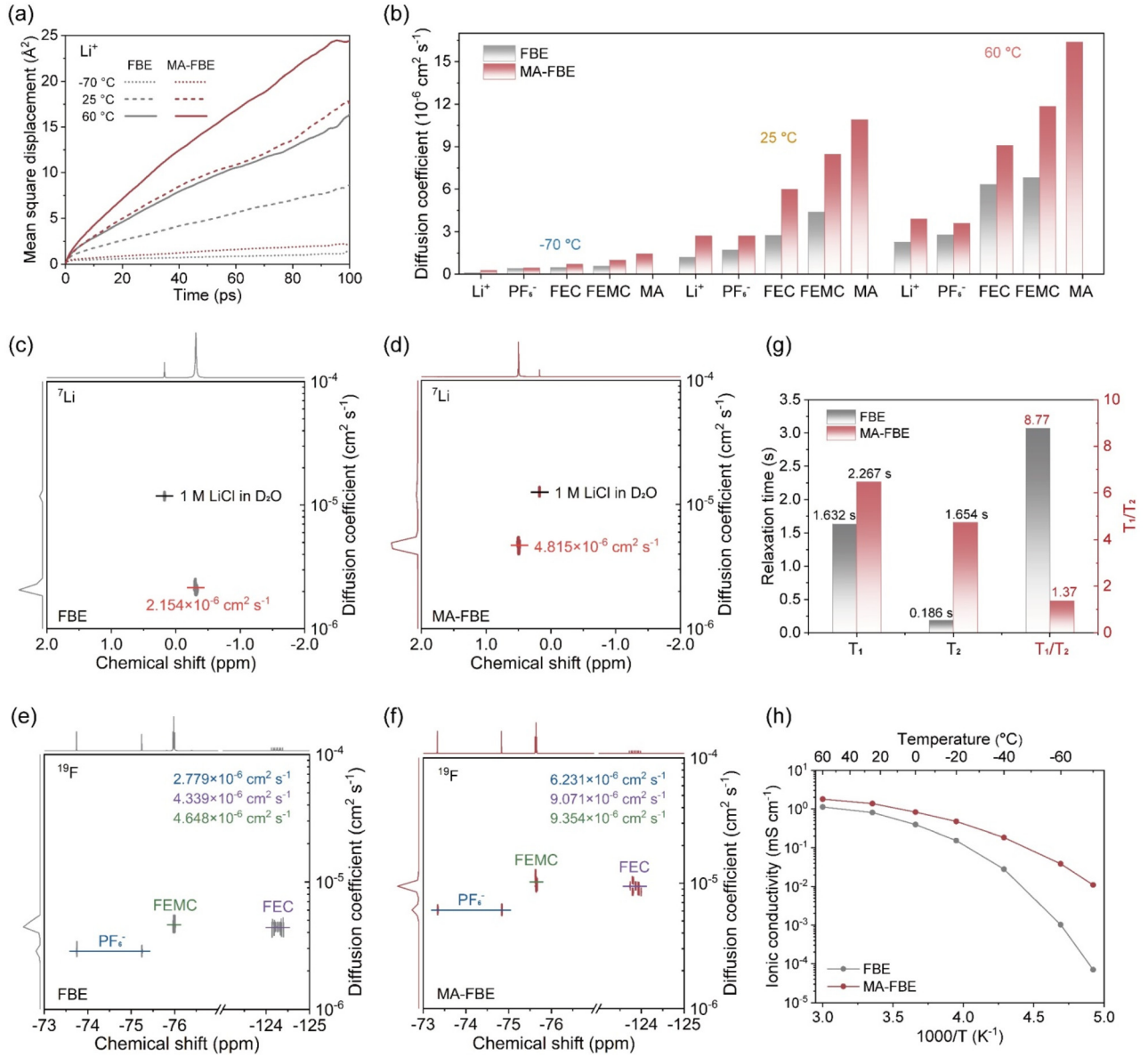

Fig. 4 Dynamic optimization of electrolyte solvation structure. (a) MSD curves of Li^+ as a function of simulation time in the FBE and MA-FBE electrolytes at −70 °C, 25 °C, and 60 °C; (b) calculated diffusion coefficients of different species in the FBE and MA-FBE electrolytes at −70 °C, 25 °C, and 60 °C; ^{7}Li DOSY-NMR spectra of the (c) FBE and (d) MA-FBE electrolytes; ^{19}F DOSY-NMR spectra of the (e) FBE and (f) MA-FBE electrolytes; (g) comparison of T_1, T_2 and T_1/T_2 in the FBE and MA-FBE electrolytes; (h) the relationship between ionic conductivity and temperature for the FBE and MA-FBE electrolytes.

compared to FBE, indicating the role of MA incorporation in boosting solvation dynamics.

For experimental validation, diffusion-ordered spectroscopy nuclear magnetic resonance (DOSY-NMR) was employed to measure the D values of the components (Fig. 4c–f and S15).[56–58] MA-FBE exhibited a 2.24-fold increase in Li^+ diffusivity (4.815×10^{-6} cm^2 s^{-1} *vs.* 2.154×10^{-6} cm^2 s^{-1} for FBE), with similar enhancements for PF_6^- (2.24-fold), FEC (2.09-fold), and FEMC (2.01-fold) species (Fig. S16). These results align with MA-induced solvation restructuring of fluorinated electrolytes. Further insights emerged from ^{7}Li NMR relaxation analysis (Fig. 4g and S17). MA-FBE displayed elevated longitudinal (T_1) and transverse (T_2) relaxation times, reflecting accelerated dynamic exchange within the Li^+ solvation shell.[59,60] The T_1/T_2 ratio for MA-FBE (1.37) approached unity, indicating fast, isotropic motions akin to an ideal liquid-like state. In contrast, FBE exhibited a higher ratio (8.78), characteristic of sluggish dynamics and anion-aggregated, "solid-like" solvation structures.[61] Wide-temperature ionic conductivity measurements from −70 °C to 60 °C further confirmed the macroscopic transport superiority of MA-FBE (Fig. 4h). The MA-FBE electrolyte achieved 1.78 mS cm^{-1} at 60 °C and retained 0.011 mS cm^{-1} at

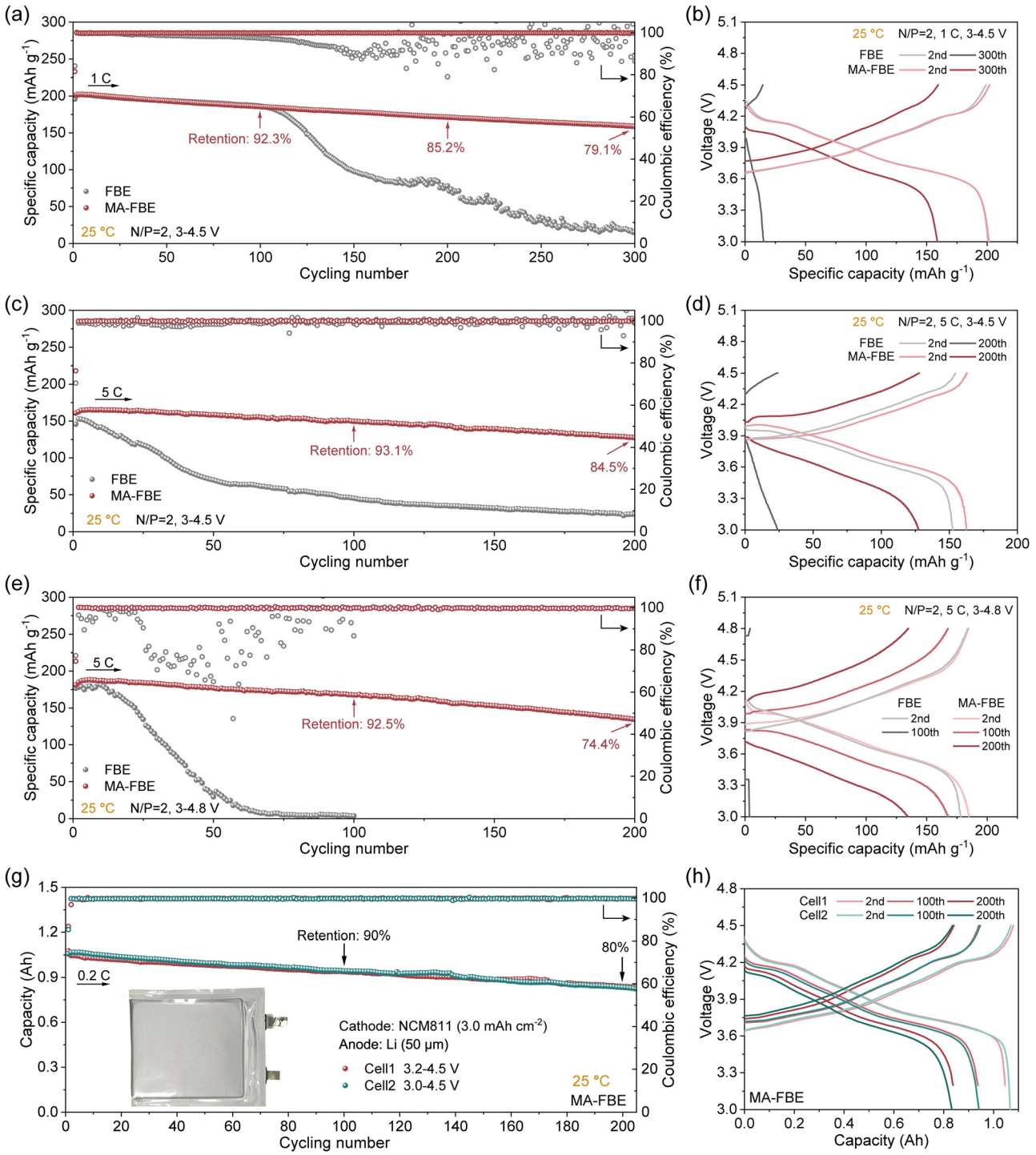

Fig. 5 High-voltage performance of NCM811||Li full cells at RT. (a) Cycling performance at 1C and (b) corresponding specific capacity–voltage curves; (c) cycling performance at 5C and (d) corresponding specific capacity–voltage curves under a 4.5 V cut-off voltage; (e) cycling performance at 5C and (f) corresponding specific capacity–voltage curves under a 4.8 V cut-off voltage for coin cells with the FBE and MA-FBE electrolytes; (g) cycling performance and (h) corresponding specific capacity–voltage curves for Ah-scale pouch cells with the MA-FBE electrolyte.

−70 °C, which represented a three-order-of-magnitude enhancement over FBE. Differential scanning calorimetry (DSC) measurements (Fig. S18) confirmed that both electrolytes maintain a stable liquid phase across the full test temperature range of −70 °C to 60 °C, eliminating electrolyte solidification as a potential cause of the conductivity gap. This pronounced performance enhancement therefore originates entirely from the dual regulation of the electrolyte solvation

structure by MA molecules: (i) weak repulsion promotes spatial homogeneity, while (ii) high mobility accelerates solvation reconfiguration, collectively enabling rapid Li^+ transport in bulk electrolytes.

2.4. Electrochemical performance of NCM811||Li full cells

To assess the practical performance of MA-FBE, we assembled NCM811||Li full cells with a low N/P ratio of 2 under demanding operational conditions, including high voltages, elevated rates, and broad temperature ranges. At room temperature (RT), cycling performance was conducted at 1C (Fig. 5a and b), 2C (Fig. S19), and 5C (Fig. 5c and d) with an upper cut-off voltage of 4.5 V. The FBE cell displayed rapid capacity degradation, fading significantly after ~105 cycles at 1C and failing within just 3 cycles at 5C. In stark contrast, the MA-FBE cell exhibited remarkable stability, retaining 79.1% and 78.8% after 300 cycles at 1C and 2C, respectively, and 84.5% after 200 cycles at 5C. The MA-FBE cell also demonstrated high-rate performance. Even at 10C, the MA-FBE cell still maintained 142.8 mAh g^{-1}, while the FBE cell only delivered a capacity of 84.5 mAh g^{-1} (Fig. S20).

When the cut-off voltage was increased to 4.8 V, MA-FBE further demonstrated its superiority, boosting the cell to maintain 92.5% capacity retention after 100 cycles and 74.4% after 200 cycles at 5C. In contrast, the FBE cell suffered abrupt failure from the 10th cycle (Fig. 5e and f). Linear sweep voltammetry (LSV) measurements (Fig. S21) further validate the high-voltage compatibility of MA-FBE, which is consistent with its superior cycling performance at 4.8 V. This enhanced stability stems from the mechanically robust yet flexible organic–inorganic hybrid CEI formed in the MA-FBE electrolyte, which effectively suppresses interfacial side reactions. This unique interfacial feature thus endows the MA-FBE-based coin cell with a low N/P ratio of 2 with exceptional long-term cycling stability under high-voltage and high-rate conditions, enabling the cell to maintain stable electrochemical performance during prolonged cycling without abrupt capacity fading or interfacial deterioration. Two parallel Ah-level NCM811 (3.0 mAh cm^{-2})||Li (50 μm) pouch cells with different electrolyte usages (11.5 and 5.7 g Ah^{-1}) were then assembled. The pouch cell exhibited an energy density of 275.9 Wh kg^{-1} (5.7 g Ah^{-1}). It maintained a capacity of ~90% after 100 cycles at 0.2C, with no obvious gas evolution or pouch swelling observed after the entire cycling process, which directly verifies the favorable long-term safety of the MA-FBE electrolyte in practical battery operation, demonstrating the effectiveness of the developed MA-FBE in stabilizing high-voltage LMBs (Fig. 5g and h).

As demonstrated by its excellent wide-temperature performance, the Li^+ transport kinetics of MA-FBE have been substantially enhanced. Fig. 6a and b compare the discharge capacity–voltage profiles of cells using FBE and MA-FBE at a current density of 0.1C (identical-condition charge and 0.05C discharge profiles in Fig. S22). For the wide-temperature dis-

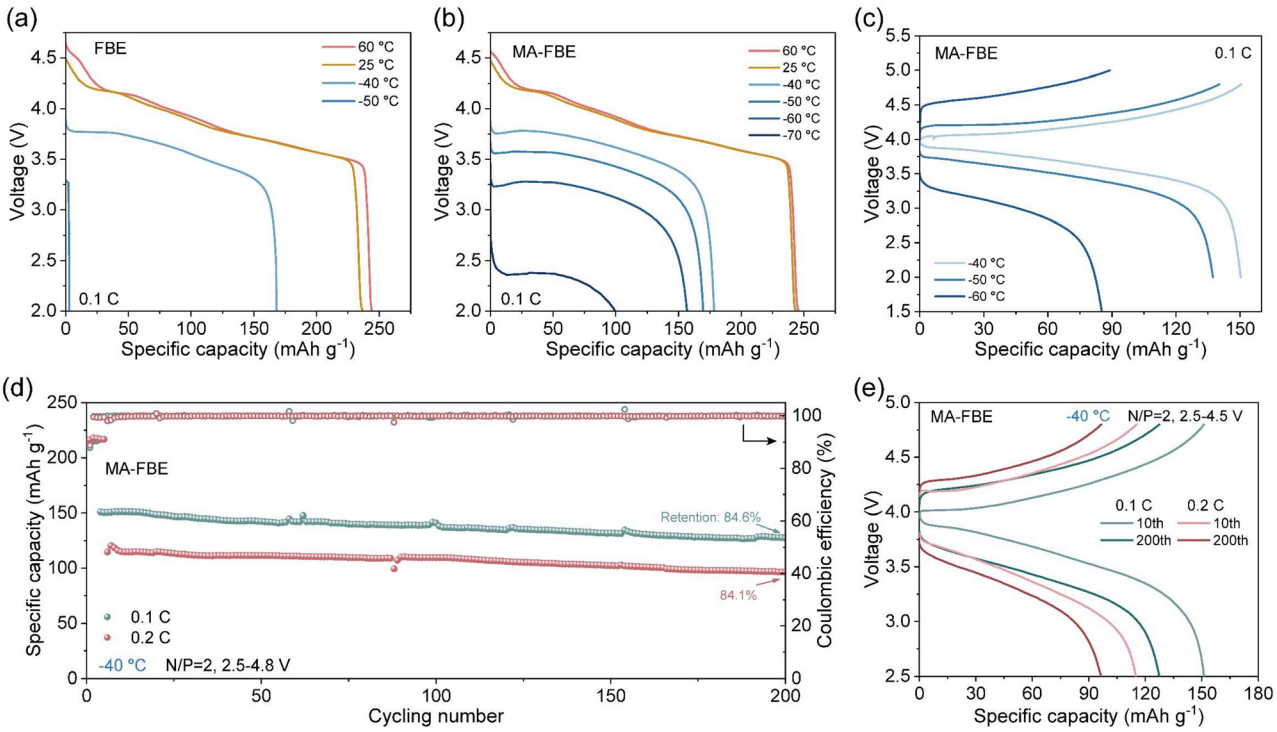

Fig. 6 Wide-temperature electrochemical performance of NCM811||Li full cells. Specific capacity–voltage curves for cells with the (a) FBE and (b) MA-FBE electrolytes charged at RT and discharged at 60, 25, −40, −50, −60, and −70 °C; (c) specific capacity–voltage curves for cells with the MA-FBE electrolyte charged and discharged at −40, −50, and −60 °C; (d) cycling performance at −40 °C at 0.1C and 0.2C and (e) corresponding specific capacity–voltage curves.

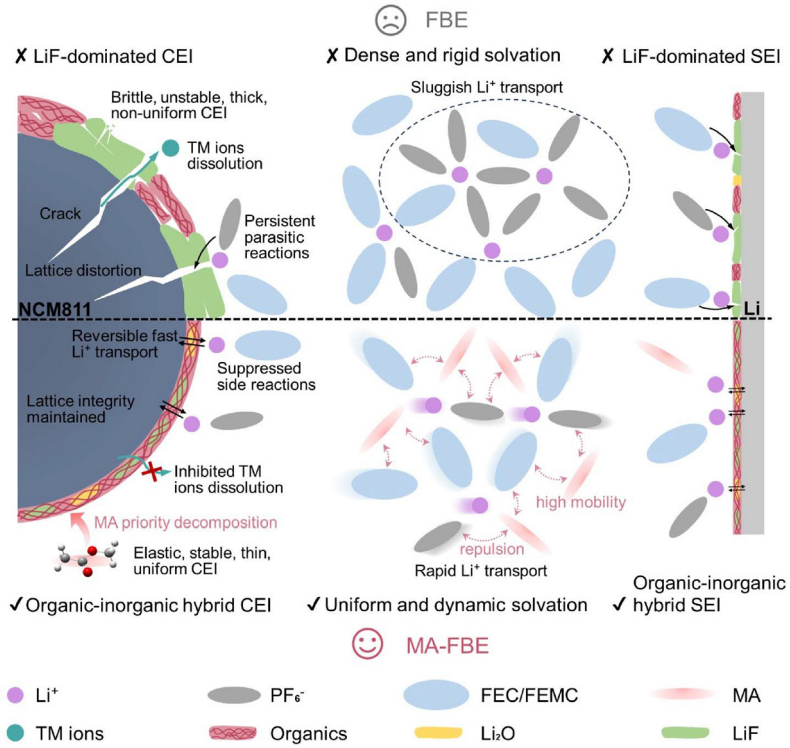

Fig. 7 Schematic diagram of MA-mediated electrolyte solvation structure regulation and EEI modulation mechanism.

charge performance tests, all cells were initially charged to 4.5 V at 0.5C at room temperature, then the thermostatic chamber was set to each target temperature for cell discharge at 0.1C. The FBE cell delivered capacities of 244.8, 237.0, and 168.1 mAh g^{-1} at 60 °C, 25 °C, and −40 °C, respectively, but failed to operate below −40 °C. In contrast, the MA-FBE cell exhibited superior performance, retaining capacities of 246.0, 243.5, 178.4, 169.8, 159.6, and 99.1 mAh g^{-1} at 60 °C, 25 °C, −40 °C, −50 °C, −60 °C, and −70 °C, respectively. Even under both charging and discharging conditions at 0.1C, the MA-FBE cell exhibited high reversible capacities of 150.3 (−40 °C), 137.3 (−50 °C), and 85.3 mAh g^{-1} (−60 °C), respectively (Fig. 6c). This improvement arises not only from the low viscosity of MA but also from its weak repulsive interactions with fluorinated solvents and anions. Such a "weak repulsion-high mobility" synergy of MA effectively loosens the compact solvation structure, thereby accelerating the kinetics of Li^+ transport. The cycling stability at −40 and 60 °C further highlights the advantages of MA-FBE. At −40 °C, the MA-FBE cell can still stabilize the cycle and maintain capacity retentions of 84.6% and 84.1% after 200 cycles at 0.1C and 0.2C, respectively (Fig. 6d and e). This outstanding cycling stability at low temperature highlights the excellent chemical stability of the MA-FBE electrolyte, which resists parasitic reactions even under prolonged low-temperature cycling. Moreover, MA decomposition enriches the organic components of CEI and SEI layers, enhancing their stability and high-temperature cycling performance to suppress parasitic reactions. This optimized organic–inorganic hybrid interphase also endows the MA-FBE-based cells with favorable long-term safety during high-temperature cycling at 60 °C, with no electrolyte leakage or abnormal thermal behavior observed throughout the cycling process, which is a key guarantee for the practical application of the electrolyte.

In addition to breakthroughs in low-temperature performance, the high-temperature cycling stability of the MA-FBE cell has also been guaranteed. At 5C and 60 °C, the MA-FBE cell maintained 79.4% capacity retention, whereas the FBE cell degraded rapidly and delivered no capacity after 100 cycles (Fig. S23). Comprehensively, the synergistic modulation of solvation structures and CEIs enabled by the MA cosolvent is schematically illustrated in Fig. 7, elucidating molecular-level interactions that enhance interfacial stability and Li^+ transport kinetics. The developed MA-FBE outperforms state-of-the-art electrolytes in terms of wide-temperature operation, high-voltage tolerance, and high-rate capability, as benchmarked in Table S3, compared to LMBs.

3. Conclusions

This study aimed to explore the limitations of fluorinated electrolytes in producing unstable CEI and their poor performance at low temperatures. We introduced MA as a synergistic electrolyte cosolvent to improve Li^+ coordination environments. MA molecules participate in the inner Li^+ solvation sheath

because of their stronger binding energy to Li^+, while they exert weak repulsive forces on fluorinated solvents and PF_6^- anions. As a result, the organic components in the CEI layer, derived from MA decomposition, can provide elasticity to withstand a high voltage of 4.8 V. Additionally, the compact solvation structure formed by fluorinated solvents, due to the high electronegativity of fluorine, can be loosened so that ionic conductivity remains high even at ultralow temperatures of −70 °C. These structural and interfacial optimizations endow the MA-FBE-based lithium metal batteries with exceptional long-term cycling stability under harsh high-voltage, high-rate, and wide-temperature conditions. More importantly, this work establishes a new design principle for next-generation electrolytes that enhance interfacial stability and ion transport kinetics through coordinated molecular engineering of solvation structures and interphase composition, offering a universal strategy for developing future high-energy-density LMBs.

4. Methods

4.1. Materials and electrolytes

$LiPF_6$, FEC, and FEMC were purchased from Suzhou Dodo Chemical Technology Co., Ltd. MA was obtained from Shanghai Aladdin Biochemical Technology Co., Ltd. Electrolytes were prepared and stored in an argon (Ar)-filled glovebox (H_2O and O_2 <0.1 ppm). Commercial NCM811 cathodes (Shenzhen Kejing Zhida Technology Co., Ltd) for coin cells featured an areal active material loading of ∼10.5 mg cm^{-2} and a compacted density of ∼2.75 g cm^{-3}. Li metal anodes were fabricated by galvanostatic deposition (0.2 mA cm^{-2}) of a predefined lithium capacity onto Cu foil; the plated foil was subsequently disassembled from the Cu‖Li cell. All coin-type NCM811‖Li full cells had an N/P of 2. The 1 Ah stacked pouch cells (Canrd Technology Co., Ltd) utilized an NCM811 cathode with 15.12 mg cm^{-2} loading and a 50 μm Li anode, yielding an N/P of ∼3.4.

4.2. Electrochemical measurements and characterization

The CR2025 coin cells and pouch cells were assembled in an Ar-filled glove box for the electrochemical measurements. For the coin-type NCM811‖Li half cells, the configuration included Li foil (450 μm thickness), Celgard 2325 separator, and NCM811 cathode electrodes with 70 μL electrolyte. The 1C rate was defined as 200 mA g^{-1} based on the NCM811 active mass, and cells were cycled between 3.0–4.5 V. Cu‖Li cells were constructed using Li foil (450 μm), Celgard 2325 separator, and Cu foil with 50 μL electrolyte, evaluating electrochemical plating/stripping *via* discharge at 1 mA cm^{-2} to 1 mAh cm^{-2} followed by charge to 1.0 V cut-off voltage. Coin-type NCM811‖Li full cells employed lithium-plated copper (Cu) anodes (pre-electrodeposited), Celgard 2325 separator, and NCM811 cathodes (70 μL electrolyte). All charge/discharge measurements were conducted using the LAND battery testing system (CT2001A, Wuhan, China). Temperature control beyond ambient conditions (including high and low temperatures) was achieved through a thermostatic chamber.

EIS measurements were conducted using an electrochemical workstation over a frequency range of 0.01 Hz to 1 MHz with an amplitude of 10 mV. The ionic conductivity was determined using stainless steel (SS)‖SS symmetric cells and calculated according to the following equation: $\sigma = \frac{L}{R_b A}$, where L denotes the inter-electrode spacing, R_b represents the bulk electrolyte resistance, and A corresponds to the effective electrode surface area. One-dimensional ^{7}Li NMR spectra were acquired using a JEOL JNM-ECA600 spectrometer operating at 600 MHz. DOSY-NMR measurements for ^{7}Li and ^{19}F nuclei, along with T_1 and T_2 analyses for ^{7}Li, were conducted on a Bruker AVANCE NEO 500 MHz spectrometer. XPS measurements were acquired using a ULVAC-PHI Quantera II scanning XPS microprobe. ToF-SIMS measurements were performed on a PHI nano TOF II instrument (ULVAC-PHI, Japan). SEM characterization was performed using a FEI Sirion 200 field-emission microscope, while XRD analysis with Cu Kα radiation (λ = 1.5406 Å, Rigaku SmartLab diffractometer) was conducted to investigate the cycled NCM811 cathode morphology (identical to XPS specimens) and bulk crystalline structure, respectively.

4.3. MD simulations and quantum chemistry calculations

MD simulations were performed using the Forcite module in Materials Studio 2023 to analyze electrolyte systems at multiple temperatures. The FBE electrolyte system contained 125 Li^+, 125 PF_6^-, 584 FEC, and 690 FEMC molecules. The MA-FBE electrolyte system consisted of 125 Li^+, 125 PF_6^-, 350 FEC, 414 FEMC, and 631 MA molecules. All simulations employed the COMPASS III force field[62] with a time step of 1.0 femtosecond (fs). To assess the integrity of the force field parameters, an initial 50 picoseconds (ps) NPT equilibration was performed at 298.15 K using the Bussi thermostat coupled with the Berendsen barostat to sustain a pressure of 10^{-4} GPa. Following equilibration, production simulations were carried out in the NVT ensemble for 20 ps duration, with temperature control achieved through a Nosé thermostat at target values of 398.15 K, 333.15 K, 298.15 K, and 203.15 K. Subsequently, three independent 20 ps NPT simulations were conducted at 333.15 K, 298.15 K, and 203.15 K, followed by extended 100 ps NVT simulations at identical temperatures based on the equilibrated configurations from preceding NPT runs. The cumulative simulation time ensured adequate sampling for all electrolyte systems to reach thermodynamic equilibrium.

The geometry optimization, frequency calculations, energy evaluations, and electronic structure analyses of electrolyte and solvent molecules were performed using the Gaussian 16 package with the B3LYP functional[63] and the 6-311++G(d,p) triple-zeta basis set.[64] Structural visualization was conducted *via* GaussView 6.0. The surface electrostatic potential (ESP) extrema distribution and molecular orbitals, including the highest HOMO and the lowest unoccupied molecular orbital (LUMO) of the molecules listed in Table S1, were calculated.

The binding energy (ΔE) between any two components (ions, molecules, *etc.*) was calculated using the following equation: $\Delta E = E_{A+B} - E_A - E_B$, where E_A and E_B represent the sums of electronic and thermal free energies of individual ions or molecules, and E_{A+B} denotes the total energy of the complex.

Author contributions

H. Tian designed and conducted the experiments, performed calculations, analyzed data, and wrote the manuscript. Z. X. Hong, Z. H. Fang, H. C. Wu, and F. Zhao assisted with sample preparation and data collection. J. P. Wang and Y. F. Luo supervised the experimental design and revised the manuscript. All authors contributed to data interpretation and approved the final submission.

Conflicts of interest

The authors declare no conflict of interest.

Data availability

The data supporting this article have been included as part of the supplementary information (SI). Supplementary information is available. See DOI: https://doi.org/10.1039/d5eb00208g.

Additional data may be made available upon reasonable request.

Acknowledgements

This work was supported by the National Basic Research Program of China (2019YFA0705702) and the National Natural Science Foundation of China (W2441009 and 51872158).

References

1 J. Chen, D. Zhang, L. Zhu, M. Liu, T. Zheng, J. Xu, J. Li, F. Wang, Y. Wang, X. Dong and Y. Xia, *Nat. Commun.*, 2024, **15**, 3217.
2 S. Sun, K. Wang, Z. Hong, M. Zhi, K. Zhang and J. Xu, *Nano-Micro Lett.*, 2024, **16**, 35.
3 N. Zhang, T. Deng, S. Zhang, C. Wang, L. Chen, C. Wang and X. Fan, *Adv. Mater.*, 2022, **34**, 2107899.
4 L. Hou, X. Zhang, B. Li and Q. Zhang, *Angew. Chem., Int. Ed.*, 2020, **59**, 15109–15113.
5 H. M. K. Sari and X. Li, *Adv. Energy Mater.*, 2019, **9**, 1901597.
6 J. Xiao, N. Adelstein, Y. Bi, W. Bian, J. Cabana, C. L. Cobb, Y. Cui, S. J. Dillon, M. M. Doeff, S. M. Islam, K. Leung, M. Li, F. Lin, J. Liu, H. Luo, A. C. Marschilok, Y. S. Meng, Y. Qi, R. Sahore, K. G. Sprenger, R. C. Tenent, M. F. Toney, W. Tong, L. F. Wan, C. Wang, S. E. Weitzner, B. Wu and Y. Xu, *Nat. Energy*, 2024, **9**, 1463–1473.
7 M. Yeddala, L. Rynearson and B. L. Lucht, *ACS Energy Lett.*, 2023, **8**, 4782–4793.
8 Z. Piao, R. Gao, Y. Liu, G. Zhou and H. M. Cheng, *Adv. Mater.*, 2023, **35**, 2206009.
9 H. Wan, J. Xu and C. Wang, *Nat. Rev. Chem.*, 2024, **8**, 30–44.
10 Y. S. Meng, V. Srinivasan and K. Xu, *Science*, 2022, **378**, 1065.
11 N. Piao, J. Wang, X. Gao, R. Li, H. Zhang, G. Hu, Z. Sun, X. Fan, H. M. Cheng and F. Li, *J. Am. Chem. Soc.*, 2024, **146**, 18281–18291.
12 N. Zhang, T. Deng, S. Zhang, C. Wang, L. Chen, C. Wang and X. Fan, *Adv. Mater.*, 2022, **34**, 2107899.
13 H. Cheng, Z. Ma, P. Kumar, H. Liang, Z. Cao, H. Xie, L. Cavallo, H. Kim, Q. Li, Y. Sun and J. Ming, *Adv. Energy Mater.*, 2024, **14**, 2304321.
14 C. Tian, K. Qin and L. Suo, *Mater. Futures*, 2023, **2**, 012101.
15 G. A. Giffin, *Nat. Commun.*, 2022, **13**, 5250.
16 C. M. Efaw, Q. Wu, N. Gao, Y. Zhang, H. Zhu, K. Gering, M. F. Hurley, H. Xiong, E. Hu, X. Cao, W. Xu, J. G. Zhang, E. J. Dufek, J. Xiao, X. Q. Yang, J. Liu, Y. Qi and B. Li, *Nat. Mater.*, 2023, **22**, 1531–1539.
17 X. B. Guo, J. X. Tang, W. B. Xiong, X. Liu, H. Wang, T. Wu and Y. Cheng, *Front. Chem. Sci. Eng.*, 2023, **17**, 1354–1371.
18 R. Yi, K. Xu, W. Zhao, Z. Ren, Q. Dong, H. Shao, Y. Shen and L. Chen, *Angew. Chem., Int. Ed.*, 2025, e202423439.
19 H. K. Bergstrom and B. D. McCloskey, *ACS Energy Lett.*, 2024, **9**, 373–380.
20 S. Chen, J. Zheng, D. Mei, K. S. Han, M. H. Engelhard, W. Zhao, W. Xu, J. Liu and J. G. Zhang, *Adv. Mater.*, 2018, **30**, 1706102.
21 H. Xiao, X. Li and Y. Fu, *Nano-Micro Lett.*, 2025, **17**, 149.
22 Y. Yamada, J. Wang, S. Ko, E. Watanabe and A. Yamada, *Nat. Energy*, 2019, **4**, 269–280.
23 X. Liu, S. Wu, Z. Hao, L. Shang, M. Guo, J. Hou, S. Shao, H. Li, Y. Li, Y. Lu, K. Zhang, Z. Yan and J. Chen, *Angew. Chem., Int. Ed.*, 2024, **64**, e202416731.
24 Z. Wang and B. Zhang, *Energy Mater. Devices*, 2023, **1**, 9370003.
25 X. Li, F. Luo, N. Zhou, H. Adenusi, S. Fang, F. Wu and S. Passerini, *Adv. Energy Mater.*, 2025, **15**, 2501272.
26 Y. P. Chen, X. Chen, N. Yao, Z. Zheng, L. Yu, Y. C. Gao, H. B. Zhu, C. L. Wang, J. H. Yao and Q. Zhang, *Mater. Today*, 2025, **85**, 304–318.
27 S. J. Yang, N. Yao, F. N. Jiang, J. Xie, S. Y. Sun, X. Chen, H. Yuan, X. B. Cheng, J. Q. Huang and Q. Zhang, *Angew. Chem., Int. Ed.*, 2022, **61**, e202214545.
28 Y. Wu, X. Feng, X. Liu, X. Wang, D. Ren, L. Wang, M. Yang, Y. Wang, W. Zhang, Y. Li, Y. Zheng, L. Lu, X. Han, G. L. Xu, Y. Ren, Z. Chen, J. Chen, X. He, K. Amine and M. Ouyang, *Energy Storage Mater.*, 2021, **43**, 248–257.
29 Z. Li, Y. Chen, X. Yun, P. Gao, C. Zheng and P. Xiao, *Adv. Funct. Mater.*, 2023, **33**, 2300502.

30 Y. H. T. Tran, K. An, D. T. T. Vu and S. W. Song, *ACS Energy Lett.*, 2024, **10**, 356–370.
31 C. Liu, K. Ren, S. Wu, Y. Zhang, H. W. Li, M. Yao, Z. Jiang and Y. Li, *Nano Lett.*, 2025, **25**, 7762–7769.
32 Z. Li, L. Wang, X. Huang and X. He, *Small*, 2024, **20**, 2305429.
33 G. Chemical, *J. Am. Chem. Soc.*, 1932, **54**, 3570–3582.
34 S. Noorizadeh and E. Shakerzadeh, *J. Mol. Struct.*, 2009, **920**, 110–113.
35 Z. Qiu, Y. Cui, L. Zhou, B. Li, X. Gao, X. Li and P. Liu, *Energy Storage Mater.*, 2025, **76**, 104122.
36 X. Fan, X. Ji, L. Chen, J. Chen, T. Deng, F. Han, J. Yue, N. Piao, R. Wang, X. Zhou, X. Xiao, L. Chen and C. Wang, *Nat. Energy*, 2019, **4**, 882–890.
37 Z. Wang, R. Han, D. Huang, Y. Wei, H. Song, Y. Liu, J. Xue, H. Zhang, F. Zhang, L. Liu, S. Weng, S. Lu, J. Xu, X. Wu and Z. Wei, *ACS Nano*, 2023, **17**, 18103–18113.
38 Y. Jie, X. Ren, R. Cao, W. Cai and S. Jiao, *Adv. Funct. Mater.*, 2020, **30**, 1910777.
39 J. Liu, S. Ihuaenyi, R. Kuphal, J. Salinas, L. Xie, L. Yang, U. Janakiraman, M. E. Fortier and C. Fang, *J. Electrochem. Soc.*, 2023, **170**, 010535.
40 W. Cai, Y. Deng, Z. Deng, Y. Jia, Z. Li, X. Zhang, C. Xu, X. Q. Zhang, Y. Zhang and Q. Zhang, *Adv. Energy Mater.*, 2023, **13**, 2301396.
41 L. Su, E. Jo and A. Manthiram, *ACS Energy Lett.*, 2022, **7**, 2165–2172.
42 L. Deng, L. Dong, Z. Wang, Y. Liu, J. Zhan, S. Wang, K. P. Song, D. Qi, Y. Sang, H. Liu and H. Chen, *Adv. Energy Mater.*, 2024, **14**, 2303652.
43 B. Zhang, X. Wu, H. Luo, H. Yan, Y. Chen, S. Zhou, J. Yin, K. Zhang, H. G. Liao, Q. Wang, Y. Zou, Y. Qiao and S. G. Sun, *J. Am. Chem. Soc.*, 2024, **146**, 4557–4569.
44 S. Zhou, J. Yang, C. Zhen, M. D. Gu and M. Shao, *Adv. Mater.*, 2024, 2410199.
45 J. B. Goodenough and Y. Kim, *Chem. Mater.*, 2010, **22**, 587–603.
46 Z. Qin, T. Zhang, X. Gao, W. Luo, J. Han, B. Lu, J. Zhou and G. Chen, *Adv. Mater.*, 2024, **36**, 2307091.
47 Q. Huang, X. Zhang, X. Lv, X. Wang, W. Wen, F. Wu, R. Chen and L. Li, *Small*, 2023, **19**, 2302086.
48 F. Friedrich, B. Strehle, A. T. S. Freiberg, K. Kleiner, S. J. Day, C. Erk, M. Piana and H. A. Gasteiger, *J. Electrochem. Soc.*, 2019, **166**, A3760–A3774.
49 S. Arrhenius, *Z. Phys. Chem.*, 1889, **4**, 226–248.
50 H. Tian, Z. Hong, Z. Fang, Y. Luo, H. Wu, F. Zhao, Q. Li, S. Fan and J. Wang, *Adv. Sci.*, 2024, **12**, 2409259.
51 Q. K. Zhang, X. Q. Zhang, J. Wan, N. Yao, T. L. Song, J. Xie, L. P. Hou, M. Y. Zhou, X. Chen, B. Q. Li, R. Wen, H. J. Peng, Q. Zhang and J. Q. Huang, *Nat. Energy*, 2023, **8**, 725–735.
52 M. A. L. Marques, J. Vidal, M. J. T. Oliveira, L. Reining and S. Botti, *Phys. Rev. B: Condens. Matter Mater. Phys.*, 2011, **83**, 035119.
53 T. N. Tran, X. Cao, Y. Xu, P. Gao, H. Zhou, F. Guo, K. S. Han, D. Liu, P. M. L. Le, J. M. Weller, M. H. Engelhard, C. Wang, M. S. Whittingham, W. Xu and J. G. Zhang, *Adv. Funct. Mater.*, 2024, **34**, 2407012.
54 A. Einstein, *Ann. Phys.*, 1905, **322**, 549–560.
55 J. Quirk, M. Rothmann, W. Li, D. Abou-Ras and K. P. McKenna, *Appl. Phys. Rev.*, 2024, **11**, 011308.
56 C. C. Su, M. He, R. Amine, T. Rojas, L. Cheng, A. T. Ngo and K. Amine, *Energy Environ. Sci.*, 2019, **12**, 1249–1254.
57 Y. Wang, Z. Li, W. Xie, Q. Zhang, Z. Hao, C. Zheng, J. Hou, Y. Lu, Z. Yan, Q. Zhao and J. Chen, *Angew. Chem., Int. Ed.*, 2024, **63**, e202310905.
58 Y. Zhang, F. Li, Y. Cao, M. Yang, X. Han, Y. Ji, K. Chen, L. Liang, J. Sun and G. Hou, *Adv. Funct. Mater.*, 2024, **34**, 2315527.
59 M. Ohuchi, P. Meadows, H. Horiuchi, Y. Sakai and K. Furihata, *Polym. J.*, 2000, **32**, 760–770.
60 S. Appelt, H. Kühn, F. W. Häsing and B. Blümich, *Nat. Phys.*, 2006, **2**, 105–109.
61 C. P. Fonseca, L. P. Montezinho, G. Baltazar, B. Layden, D. M. Freitas, C. F. G. C. Geraldes and M. M. C. A. Castro, *Met.-Based Drugs*, 2000, **7**, 357–364.
62 R. L. C. Akkermans, N. A. Spenley and S. H. Robertson, *Mol. Simul.*, 2021, **47**, 540–551.
63 P. J. Stephen, F. J. Devlin, C. F. Chabalowski and M. J. Frisch, *J. Phys. Chem.*, 1994, **98**, 11623–11627.
64 R. Krishnan, J. S. Binkley, R. Seeger and J. A. Pople, *J. Chem. Phys.*, 1980, **72**, 650–654.